ELSEVIER ELSEVIER

Contents lists available at ScienceDirect

Computer-Aided Design

journal homepage: www.elsevier.com/locate/cad



Spherical optimal transportation*,***

Li Cui ^a, Xin Qi ^b, Chengfeng Wen ^b, Na Lei ^{c,e,*}, Xinyuan Li ^b, Min Zhang ^d, Xianfeng Gu ^{b,e}



- ^a School of Mathematical Science, Beijing Normal University, Beijing, China
- ^b Computer Science Department, Stony Brook University, Stony Brook, NY, USA
- ^c DUT-RU ISE, Dalian University of Technology, Dalian, China
- ^d Center of mathematical sciences and applications, Harvard University, Boston, USA
- ^e Beijing Advanced Innovation Center for Imaging Theory and Technology, Beijing, China

ARTICLE INFO

Article history: Received 26 April 2019 Accepted 4 May 2019

Keywords: Optimal transport Area-preserving mapping Spherical geometry Surface parameterization

ABSTRACT

Optimal mass transportation (OT) problem aims at finding the most economic way to transform one probability measure to the other, which plays a fundamental role in many fields, such as computer graphics, computer vision, machine learning, geometry processing and medical imaging. Most existing algorithms focus on searching the optimal transportation map in Euclidean space, based on Kantorovich theory or Brenier theory. This work introduces a novel theoretic framework and computational algorithm to compute the optimal transportation map on the sphere. Constructing with a variational principle approach, our spherical OT map is carried out by solving a convex energy minimization problem and building a spherical power diagram.

In theory, we prove the existence and the uniqueness of the spherical optimal transportation map; in practice, we present an efficient algorithm using the variational framework and Newton's method. Comparing to the existing approaches, this work is more rigorous, efficient, robust and intrinsic to the spherical geometry. It can be generalized to the hyperbolic geometry or to higher dimensions.

Our experimental results on a variety of models demonstrate efficacy and efficiency of the proposed method. At the same time, our method generates diffeomorphic, area-preserving, and seamless spherical parameterization results.

© 2019 Elsevier Ltd. All rights reserved.

1. Introduction

1.1. Motivation

Mesh parameterization. Mesh parameterization refers to the process of mapping a surface onto a canonical domain, which plays a fundamental role in computer graphics and geometry processing. In general, mesh parameterization will unavoidably introduce distortions, angle distortion and area distortion. Typically, parameterization methods emphasize the importance of angle preservation, which may induce huge area distortion and

cause numerical unreliability. For many applications in graphics, such as normal map and texture map, it is highly desirable to develop area-preserving parameterization algorithms. However, compared to conformal parameterizations, area-preserving parameterizations are much less studied in the literature [1,2].

Most parameterization algorithms can only handle topological disks, namely genus zero surfaces with single boundary. In order to process closed meshes, such as topological spheres, the mesh needs to be partitioned into a collection of simply connected patches, before each patch can be parameterized individually. This will introduce severe discontinuities along the boundaries of the patches. In practice it is valuable to design global parameterization methods, that can handle the whole closed meshes without partitioning.

The goal of this paper is to develop a novel spherical area preserving parameterization method based on optimal mass transport theory, that maps any genus zero closed mesh onto the unit sphere without area distortion nor slicing the mesh open.

Optimal mass transportation. Optimal transportation is well known for the ability to transfer one probability measure to another with the least cost and has become a powerful tool for both theoretic development and engineering applications.

ফি No author associated with this paper has disclosed any potential or pertinent conflicts which may be perceived to have impending conflict with this work. For full disclosure statements refer to https://doi.org/10.1016/j.cad. 2019.05.024.

^{*} Corresponding author at: DUT-RU ISE, Dalian University of Technology, Dalian China

E-mail addresses: licui@bnu.edu.cn (L. Cui), xinqi@cs.stonybrook.edu (X. Qi), chwen@cs.stonybrook.edu (C. Wen), nalei@dlut.edu.cn (N. Lei), xli@cs.stonybrook.edu (X. Li), mzhang@math.harvard.edu (M. Zhang), gu@cs.stonybrook.edu (X. Gu).

Optimal transport has intrinsic relations with many other branches in mathematics. For example, Brenier's theory [3] focuses on finding the optimal transportation map with L^2 cost and reduces the problem to Monge–Ampere equation, which is equivalent to the Alexandrov theory [4] in convex geometry. Optimal transport has been applied for medical imaging applications [5,6]. Recently, optimal transport itself has been applied in data sciences, especially Wasserstein distance is used for constructing generative adversarial networks [7,8].

Optimal transportation theory has been applied for surface and volume parameterizations as well. Dominitz and Tannan-baum proposed a spherical area-preserving parameterization method in [9], which is based on the fluid mechanics view of the optimal mass transportation theory, and uses gradient flow method to optimize an energy function. The method is implemented iteratively and requires many variables, resulting in complicated computation and slow convergence.

Recently, semi-discrete optimal mass transportation map has been introduced for surface and volume parameterization by Levy [10], Su [11] and Su [12]. This method is also generalized to compute angle–area-distortion balancing parameterization in [13]. These methods are based on the intrinsic relation between optimal transportation and the convex geometry, and formulated as a variational framework and reduced to a convex optimization problem with O(n) variables [14].

Unfortunately, the method introduced in [11,13] is based on Euclidean geometry. For spherical mapping, it maps the unit sphere onto the plane either by using stereo-graphic projection or by slicing into two disks, and converts the spherical optimal transportation map into a Euclidean one. The solution heavily depends on the choice of the north pole, therefore, the method is not intrinsic.

Proposed method. In this work we propose a novel method for computing spherical optimal transportation maps, which is intrinsic to the spherical geometry. It generalizes the theory of semi-discrete optimal transportation in Euclidean background geometry [14] to the spherical background geometry. Both methods are variational, with convex energies and the Hessian matrices have explicit geometric interpretation. Furthermore, both methods require only O(n) variables and can apply Newton's method directly.

Similar to the semi-discrete optimal transportation map method in Euclidean geometry [10,14], the spherical optimal transportation map is also given by a spherical power diagram, the power can be found by a convex optimization, the existence and the uniqueness of the solutions are claimed in Theorems 1, 2 and 4. The gradient and the Hessian of the energy have explicit geometric meanings as claimed in Lemmas 3, 4, and Eq. (17). Due to the nature of spherical geometry, all the formulations are more complicated than Euclidean counter parts; furthermore, if we let the variables go to infinitesimal, the spherical formula converges to Euclidean ones asymptotically.

Comparing to the existing spherical area-preserving algorithms, the proposed method is based on Newton's method, therefore much more efficient than Dominitz and Tennanbaum's algorithm [9]; our method is intrinsic to the spherical geometry, independent of the choice of the north pole, hence more robust than Su et al.'s algorithm in [11]. The experimental results demonstrate the efficiency and efficacy of the method, such that the spherical area-preserving map can efficiently generate the diffeomorphic, area-preserving, and seamless parameterizations of large models.

1.2. Our contribution

We summarize our contributions in this paper as follows:

- Generalize the Euclidean semi-discrete optimal transport theory to spherical setting via spherical power diagram;
- Construct area preserving mapping from topological spheres to unit spheres without slicing the surface into patches or stereo-graphic projection, leading to an efficient, robust and accurate algorithm based on rigorous mathematical theory.

2. Prior work

Mesh parameterization has been a vastly popular research topic for decades, resulting in the abundant literature in this area, and a thorough survey is beyond the scope of current work. We will focus on the works most directly related and recommend the readers [15–17] for more comprehensive details.

2.1. Optimal transport theory

Regarding optimal transport (OT) theory, approaches based on Monge–Kantorovich theory was first introduced as a linear programming problem in [18,19]. Image registration and warping is an intuitive application based on linear programming. Haker et al. proposed to use OT for general image registration, with the global optimization. For 3D image registration, a method was proposed in [20] stating the importance to find efficient numerical methods to deal with the expensive computation. [9] uses OT for texture mapping purpose by starting with an angle-preserving mapping between a topological sphere and the unit sphere, via a gradient flow with multiple level of resolutions to accelerate the convergence.

Some other researches are based on Monge-Brenier theory [3]. De Goes et al. proposed to use OT for 2D shape reconstruction and simplification [21], as well as formulated the capacityconstrained Voronoi tessellation as an optimal transport problem for blue noise processing purpose [22]. A multi-scale approach to solve the optimal transport problem was proposed in [23]. Most of these researches are focusing on 2D image registration and processing, while there are some other researches dealing with 3D surfaces. Incorporating with the conformal mapping method, the equiareal mapping can optimize the angle distortion at the same time [9,11,24]. To compute the area-preserving brain mapping, [5] proposed to first map the brain, which is a topological sphere, to unit disk parameter domain. This work was later improved with a divide-and-conquer scheme in [13] by first slicing the sphere into two topological disks and using conformal welding technique to glue the two hemispheres to cover the entire complex plane, including the infinity point. Heat Kernel was used for approximation in [25,26] to compute Wasserstein distances.

In our approach, we compute the power diagram on the unit sphere without ever slicing or removing triangle faces from the surface, making our method intrinsic and independent of the locus of the slicing introduced in [5,13].

2.2. Spherical parameterization

Spherical parameterization is a worthwhile approach in computer graphics for surface matching, morphing, and texture mapping. In particular, as the cortical surfaces are usually represented by a closed genus 0 surface, spherical map becomes valuable

for anatomical analysis [27–29]. Recently, a number of spherical parameterization methods aim to minimize the parametric distortion. The conventional consideration is either about angle distortion or area distortion.

To minimize the angle distortion, many of the spherical parameterizations mimic angle-preserving (conformal) maps. Now we briefly summarize some of the work. Haker et al. [30] approximated the conformal map over the sphere based on the procedure: remove one triangular face, then map the remaining surface onto a complex plane, and finally, map the plane to the sphere using the inverse stereographic projection. Gu and Yau [31] solved the spherical conformal mapping based on the harmonic energy minimization. While this approach may induce the undesired parameterization foldings when the input mesh contains long sharp features. To improve the bijectivity in [31,32], Lai et al. [33] propose a folding removal iteration by taking advantages of the weighted Laplace-Beltrami eigenprojection. Lefévre and Auzias [34] have recently considered the Laplace-Beltrami eigenfunctions and got an approach faster than that of [33]. However, the flipped triangular faces may be obtained due to the irregularities of the input mesh. Aigerman and Lipman [35], according to the harmonic energy method, constructed a seamless bijection by flattening the topological sphere to tile the infinite plane periodically. Curvature flow, redistributes the Gaussian curvature [36] or the mean curvature [37], is another kind of procedure to accomplish the conformal spherical map.

There exist some tasks that show a compromise between the area and angle distortion. For example, Friedel et al. [38] derived the harmonic energy minimization methods of planar parameterizations to sphere while blended several measures for controlling the area and angle distortion. Zayer et al. solved the scalar quasiharmonic equation to improve the area distortion in [39]. First, the input mesh is cut along a line connecting the user prescribed poles; the initial map is then found by solving a Laplace equation in the curvilinear coordinates. The parameterization distortion is then reduced using a variant of quasi-harmonic maps, and finally, a local smoothing is performed along the seam to diminish the distortion.

Some of the spherical parameterizations, however, do not explicitly deal with the distortion issues. Grimm [40] built a patch embedding relied on the hierarchical B-splines. The overlap of the patches is blended together to get the surface embedding as a whole. Praun and Hoppe [41] proposed an algorithm which progressively embeds a surface onto a sphere while minimizing the stretch norm. Asirvatham et al. [42] solved a constrained spherical parameterization based on the approach in [41]; the feature points are given manually and the alignment is enforced on the coarsest resolution on the sphere. Gotsman et al. [43] formulated the method of spherical barycentric coordinates based on the Tutte's embedding. The spherical map can be solved by a nonlinear system of quadratic equations. Saba et al. [44] improved the efficiency of this system.

3. Background

3.1. Spherical geodesics and cosine law

A great circle of S^2 is a circle which intersects S^2 with a plane passing through the center. Geodesics are portion of some great circles on sphere. The geodesic distance between two points p, q on S^2 is measured by the shortest arc length between them: $d_{S^2}(p,q) = \cos^{-1}\langle p,q\rangle$. Consider the points A,B,C of a spherical triangle Δ on S^2 , as shown in Fig. 1. Let a,b,c be the subtended

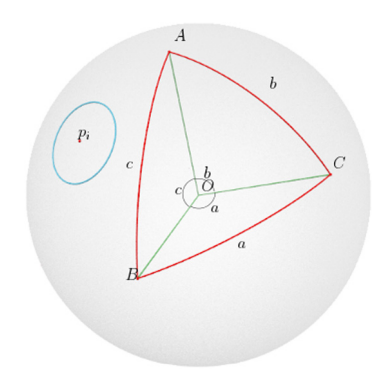


Fig. 1. Triangle and circle on unit sphere.

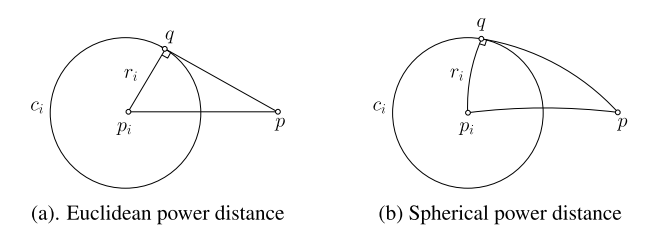


Fig. 2. Geometric interpretation to Euclidean and Spherical power distances.

angles at the center of S^2 . In fact, a, b, c also measure the geodesic distances $d_{S^2}(B, C)$, $d_{S^2}(C, A)$, and $d_{S^2}(A, B)$.

Given a point p_i on S^2 and $0 \le r_i \le \pi/2$. A geodesic circle c_i is defined by $c_i = \{p \in S^2 \mid d_{S^2}(p, p_i) = r_i\}$ where p_i is the center and r_i is the radius.

Let A, B, C also denote the angles at A, B, C respectively. The area of triangle on the sphere is

$$Area(\triangle) = A + B + C - \pi$$

Let a, b, c be the subtended angles at the center of S^2 . We have spherical cosine laws:

$$\cos a = \cos b \cos c + \sin b \sin c \cos A$$

$$\cos b = \cos c \cos a + \sin c \sin a \cos B$$

$$\cos c = \cos a \cos b + \sin a \sin b \cos C$$
(1)

and spherical sine law:

$$\frac{\sin a}{\sin A} = \frac{\sin b}{\sin B} = \frac{\sin c}{\sin C}.$$
 (2)

For right triangle, suppose the angle at C is $\pi/2$. Then the area is $Area(\triangle) = A + B - \pi/2$. Sides length and angles of right triangle have following relationship:

$$\cos c = \cos a \cos b \tag{3}$$

3.2. Spherical power diagram

Suppose that we are given a set of circles $C = \{c_1, c_2, ..., c_k\}$ on S^2 , c_i is a spherical circle with center p_i and radius r_i . Similar to Euclidean power distance in Fig. 2(a), we can define the Spherical power distance as follows:

Definition 1 (*Spherical Power Distance*). Given a geodesic circle $c_i(p_i, r_i)$ and a point $p \in S^2$, the spherical power distance between p and c_i is given by

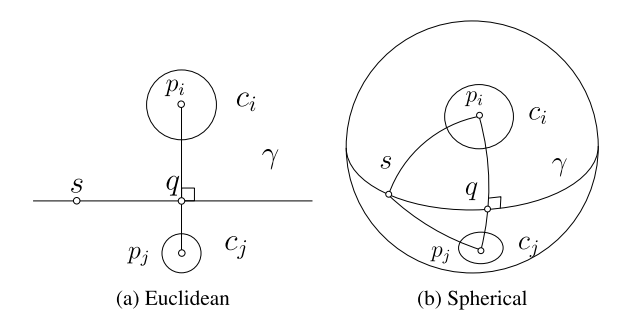


Fig. 3. Euclidean and Spherical equi-power-distance locus $LB(c_i, c_j)$.

$$pow(p, c_i) = \frac{\cos d_{S^2}(p, p_i)}{\cos r_i} = \frac{\langle p, p_i \rangle}{\cos r_i}$$

where $\langle \cdot, \cdot \rangle$ is the Euclidean dot product.

By cosines law on the sphere, $pow(p, c_i) = \cos d_{S^2}(p, q)$, where $pow(p, c_i)$ measures the length of the geodesic arc tangent to circle c_i when p is outside c_i , as shown in Fig. 2. Note that the definition is consistent when the point p is inside the circle c_i , in which case we have $pow(p, c_i) > 1$, and the power distance cannot be visualized as simple as the case that p is outside c_i . For convenience, we use $pow(p, p_i)$ to represent $pow(p, c_i)$ when the circles are implicitly provided as $\{(p_i, r_i)\}$.

Now the Spherical power diagram, shown in Fig. 4, can be defined as follows:

Definition 2 (*Spherical Power Diagram*). Given a set of geodesic circles on the unit sphere, $C = \{(p_i, r_i)\}, i = 1, 2, ...k$, the spherical power diagram is a cell decomposition of the sphere

$$S^2 = \bigcup_{i=1}^k W_i(C),$$

where each spherical power cell is given by

$$W_i(\mathcal{C}) := \{ p \in \mathcal{S}^2 | pow(p, p_i) \le pow(p, p_i), \forall j \}$$

For two circles c_i and c_j with center p_i and p_j , Laguerre bisector, shown as γ in Fig. 3, is given by

$$LB(c_i, c_i) = \{ p \in S^2 | pow(p, p_i) = pow(p, p_i) \},$$

If $p \in LB(c_i, c_i)$, p satisfies

$$\frac{\langle p, p_i \rangle}{\cos r_i} = \frac{\langle p, p_j \rangle}{\cos r_j} \tag{4}$$

The Laguerre bisector $LB(c_i, c_j)$ is a great circle, and it perpendiculars to the great circle passing through p_i and p_j . The partition of S^2 by these bisectors gives the *spherical power diagram*, as illustrated in Fig. 4. The algorithm of computing spherical power diagram is shown in [45].

Here are some terminologies we use throughout this work. Fig. 5 shows one spherical triangle $\Delta p_i p_j p_k$, where p_i , p_j and p_k are vertices with the radii r_i , r_j and r_k . o is the *power center* of the triangle with equal power distances to three vertices:

$$pow(o, p_i) = pow(o, p_i) = pow(o, p_k)$$
(5)

Through the power center draw great circular arcs perpendicular to three edges, the perpendicular feet are q_i , q_j , q_k . The three inner angles at o are θ_i , θ_j and θ_k , which determine the areas of the cells w_i , w_j and w_k respectively.



Fig. 4. Spherical power diagram. The green circles represent the set of geodesic circles and the pink line indicates the power diagram. The blue lines orthogonal to pink lines form the weighted Delaunay triangulation on the sphere. (For interpretation of the references to colour in this figure legend, the reader is referred to the web version of this article.)

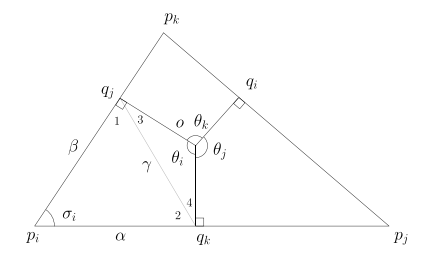


Fig. 5. One Spherical triangle and the edges of the power diagram inside the triangle.

4. Spherical semi-discrete optimal transportation

In this section, we generalize the Euclidean optimal transport to spherical situation. The main problem we want to solve is as follows:

Problem 1 (Spherical Optimal Transportation). Given an absolutely continuous probability measure μ defined on the unit sphere, and a Dirac measure $\nu = \sum_{i=1}^k \nu_i \delta_{p_i}$, $p_i \in \mathcal{S}^2$ and $\bigcup_{i=1}^k p_i$ cannot be covered by any hemisphere $\mathcal{H}_{\mathcal{S}}^2 \subset \mathcal{S}^2$ (a.k.a $\{p_i\}$ are at generic positions), such that $\mu(\mathcal{S}^2) = \sum_{i=1}^k \nu_i$, find a cell decomposition of the unit sphere, $\mathcal{S}^2 = \bigcup_{i=1}^k W_i$, such that each cell has the measure $\mu(W_i) = \nu_i$, and the mapping $W_i \mapsto p_i$ minimizes the transportation cost defined as Eq. (6).

4.1. Optimal transportation map

Given a probability density function $\mu:\mathcal{S}^2\to\mathbb{R}^+$, which is absolutely continuous with respect to the Lebesgue measure of the unit sphere. Furthermore, by scaling, we can assume the total volume is 4π , $\mu(\mathcal{S}^2)=4\pi$. The μ -volume for each power cell is defined as

$$w_i(\mathbf{h}) := \mu(W_i(\mathbf{h})) = \int_{W_i(\mathbf{h})} d\mu$$

where **h** is the height vector defined as $h_i = -\ln \cos r_i$ given that r_i is the radius of the *i*th circle c_i .

From the Kantorovich formulation, Wang [46] deduced the cost function in reflector design to be $-\log(1-\langle x,y\rangle)$. Following the same approach, we obtain the cost function for the current problem is $\log\langle x,y\rangle$. Thus, the transportation cost is defined as follows:

Definition 3 (*Spherical Transportation Cost*). Given a probability density function $\mu: \mathcal{S}^2 \to \mathbb{R}^+$, a set of geodesic circles $\mathcal{C}, \mathcal{V}(\mathcal{C})$ is a cell decomposition of \mathcal{S}^2 ,

$$S^2 = \bigcup_{i=1}^k W_i.$$

The transportation map is defined as $T: W_i \mapsto p_i$. The cost of T is defined as

$$C(T) := -\sum_{i=1}^{k} \int_{W_i(\mathbf{h})} \ln \langle p, p_i \rangle d\mu \tag{6}$$

The following lemmas show the relation between finding the spherical power diagram and minimizing transportation cost C(T).

Lemma 1 (Minimizing Transportation Cost). Given a probability density function $\mu: \mathcal{S}^2 \to \mathbb{R}^+$, a set of geodesic circles \mathcal{C} , the spherical power diagram is \mathcal{V} . For any other cell decomposition $\tilde{\mathcal{V}}$, $\mathcal{S}^2 = \bigcup_{i=1}^k \tilde{W}_i$, such that $\mu(W_i) = \mu(\tilde{W}_i)$ for all i, the transportation cost of \mathcal{V} is no greater than that of $\tilde{\mathcal{V}}$.

Furthermore, the relationship between power cell areas and power circle radii are stated in the following lemma.

Lemma 2. The power cell areas are analytic functions of circle radii.

Both proofs for Lemmas 1 and 2 can be found in the Appendix. Given the relationship of power cell areas $\{w_i\}$ and power circle radii $\{r_i\}$, along with the identity that $h_i = -\ln \cos r_i$, we consider the vector of the cell areas, $\mathbf{w} = (w_1, w_2, \ldots, w_k)$, it is obvious that the total area equals 4π , the space of all possible \mathbf{w} 's is defined as

$$\mathcal{W} \coloneqq \left\{ \mathbf{w} \middle| \sum_{i=1}^k w_i(\mathbf{h}) = 4\pi, w_i(\mathbf{h}) > 0 \right\}$$

and the space of all possible height vectors is defined as

$$\mathcal{H} := \left\{ \mathbf{h} \middle| \min_{i \in [1,k]} h_i = 0, w_i(\mathbf{h}) > 0 \right\}$$

Theorem 1 demonstrates the local rigidity property of our problem:

Theorem 1. Given a set of spherical geodesic circles $C = (c_1, c_2, \ldots, c_k)$, the spherical power diagram induces a mapping $\phi : \mathcal{H} \to \mathcal{W}$. The mapping is locally diffeomorphic.

The proof of Theorem 1 can be found in the Appendix.

Theorem 2. Suppose $\{p_1, p_2, \ldots, p_k\} \subset S^2$ is a set of points on the unit sphere at generic positions, $C = \{c_1, c_2, \ldots, c_k\}$ is a set of geodesic circles on the sphere, c_i is centered at p_i with radius $0 < r_i < \pi/2$. Let $\mathbf{h} = (h_1, h_2, \ldots, h_k)$ satisfies $h_i = -\ln \cos r_i$. C induces a power diagram, each cell area is $w_i(\mathbf{h})$, then the energy function

$$E(\mathbf{h}) = \int_{-\mathbf{h}}^{\mathbf{h}} w_1 dh_1 + w_2 dh_2 + \dots + w_k dh_k$$

is well defined on \mathcal{H} , and locally strictly convex.

In fact, if we construct a differential form $\omega = \sum_{i=1}^k w_i(\mathbf{h}) dh_i$, we will need

$$\frac{\partial w_i}{\partial h_i} = \frac{\partial w_j}{\partial h_i} \tag{7}$$

to ensure that ω is indeed a closed 1-form. Fortunately, the following lemmas will guarantee that Eq. (7) is correct.

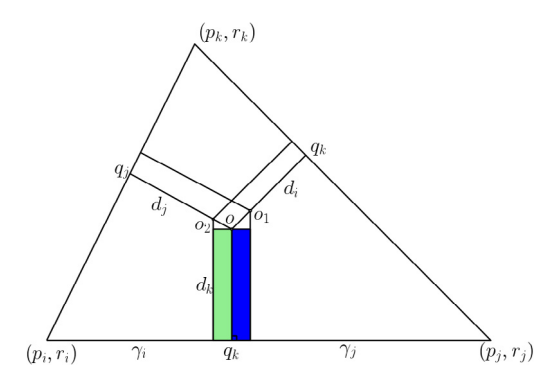


Fig. 6. Modifying r_i solely will result in the change of w_i , w_j and w_k . (For interpretation of the references to colour in this figure legend, the reader is referred to the web version of this article.)

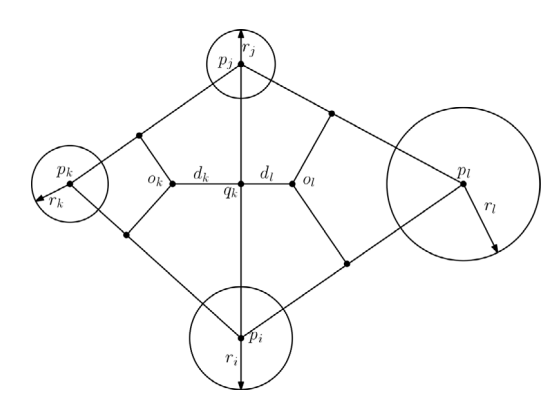


Fig. 7. Symmetry of the derivative.

Lemma 3. Let $w_i^{jk} := Area(W_i \cap \Delta p_i p_j p_k)$. The partial derivative of w_i^{jk} with respect to $h_i = -\ln \cos r_i$ is given by

$$\frac{\partial}{\partial h_i} w_j^{ik} = -\frac{R_{ijk}^2 \sin d_k}{\sin \gamma_{ij} \cos^2 d_k} \cos r_i \cos r_j \tag{8}$$

where R_{ijk} is the power distance $pow(o, p_i)$ of the triangle $\Delta p_i p_j p_k$, $\gamma_{ij} = \gamma_i + \gamma_j$. The other notations are shown in Fig. 6.

The proof of Lemma 3 and Eq. (8) can be found in the Appendix.

Now we have the Hessian matrix with elements defined in the following lemma:

Lemma 4. The power diagram constructed as mentioned above has the symmetric configuration as shown in Fig. 7, and the partial derivatives are given by

$$\frac{\partial w_i}{\partial h_j} = \frac{\partial w_j}{\partial h_i} = -\frac{\cos r_i \cos r_j}{\sin \gamma_{ij}} \left(\frac{R_l^2 \sin d_l}{\cos^2 d_l} + \frac{R_k^2 \sin d_k}{\cos^2 d_k} \right)$$
(9)

$$\frac{\partial w_i}{\partial h_i} = -\sum_{i \neq i} \frac{\partial w_i}{\partial h_j} \tag{10}$$

where o_k and o_l are the power centers of triangle $\Delta p_i p_j p_k$ and $\Delta p_j p_i p_l$, the power distances between each vertex of the two triangles to the power centers are R_k and R_l respectively, and the distances from the power centers to the common edge are d_k and d_l .

Note that for any triangle, the power distances from each vertex to the power center are identical. Also note that one of d_k and d_l can be negative (when o_l is located in triangle $\Delta p_l p_l p_k$

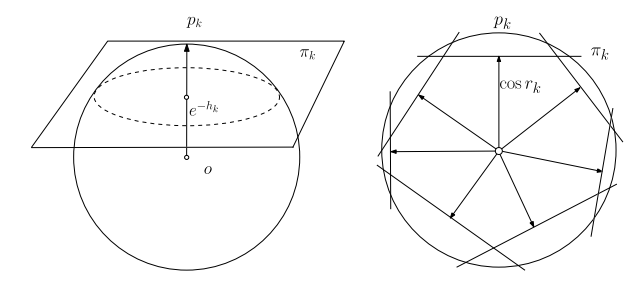


Fig. 8. Spherical power diagram and convex polyhedron construction. Note that $e^{-h_k} = \cos r_k$, and it is the euclidean distance from the sphere center O to the plane π_k .

for instance, thus $d_k > 0$, $d_l < 0$, $|d_k| > |d_l|$), but not both, making the term $\frac{\partial w_i}{\partial h_i}$ to be negative for all i and j.

Moreover, in the situation of non-constant source measure, namely $\mu=\mu(\tilde{\theta},\tilde{\phi})$, according to Eq. (25), Eq. (9) will become the following form:

$$\frac{\partial w_i}{\partial h_j} = \frac{\partial w_j}{\partial h_i} = -\frac{\cos r_i \cos r_j}{\sin \gamma_{ij}} \left(\frac{D \cdot R_l^2}{\cos^2 d_l} + \frac{C \cdot R_k^2}{\cos^2 d_k} \right)$$
(11)

where $C = \int_{d_k} \mu(\theta, \phi) \cos\theta d\theta$ and $D = \int_{d_l} \mu(\theta, \phi) \cos\theta d\theta$ and the notations are consistent with the notations Fig. 7 and Eq. (25). The (θ, ϕ) is the local coordinate chosen to satisfy that the iso- θ curve and iso- ϕ curve is orthogonal and d_k lies on the iso- ϕ curve while γ_{ij} lies on the iso- θ curve, similar to the $(\tilde{\theta}, \tilde{\phi})$ coordinate in Fig. 17. Therefore, the symmetry of the Hessian matrix is guaranteed as well.

Finally, we proved Eq. (7) and thus the differential form $\omega = \sum_{i=1}^k w_i(\mathbf{h})dh_i$ is closed. Since \mathcal{H} is simply connected, ω is exact. The energy function $E = \int \omega$ is well defined. The gradient of E is given by

$$\nabla E = (w_1, w_2, \dots, w_k)^T \tag{12}$$

The Hessian matrix element $w_{ij}=\partial w_i/\partial h_j$ in Eq. (9) is negative, and the diagonal element is defined as $w_{ii}=-\sum_{j\neq i}w_{ij}$. Therefore, the Hessian matrix is diagonal dominant in \mathcal{H} . The energy function is locally convex.

Global Rigidity Given a set of spherical circles $\mathcal{C} = \{(p_1, r_1), \ldots, (p_k, r_k)\}$, one can construct the spherical power diagram and a convex polyhedron, where the central projection of the polyhedron to the sphere gives the power diagram, hence both of the power diagram and the convex polyhedron have the same combinatorial structures. Through each spherical circle (p_i, r_i) , there is a Euclidean plane in \mathbb{R}^3 as shown in Fig. 8 where $\cos r_i = e^{-h_i}$,

$$\pi_i(p) := \langle p_i, p \rangle - \cos r_i$$
.

The plane π_i divides \mathbb{R}^3 into two half spaces, the intersection of all such half spaces containing the origin is a convex body

$$P(\mathcal{C}) := \bigcap_{i=1}^k \{ p \in \mathbb{R}^3 | \pi_i(p) < 0 \}.$$

The boundary of $P(\mathcal{C})$ is a convex polyhedron. The central projection of the convex polyhedron on the sphere gives the power diagram. The intersection between two cells $W_i \cap W_j$ is the projection image of the intersection line between π_i and π_j . Therefore the combinatorial structure of the convex polyhedron gives that of the power diagram.

Definition 4 (*Minkowski Sum*). Suppose P_1 and P_2 are sets in \mathbb{R}^n , the Minkowski sum of P_1 and P_2 is given by

$$P_1 \oplus P_2 := \{p_1 + p_2 \in \mathbb{R}^n | p_1 \in P_1, p_2 \in P_2\}.$$

The following Brunn-Minkowski inequality [47] is well known.

Theorem 3 (Brunn–Minkowski). Let $n \geq 1$ and let μ denote the Lebesgue measure on \mathbb{R}^n . Let A and B be two nonempty compact subsets of \mathbb{R}^n . Then the following inequality holds:

$$[\mu(A \oplus B)]^{\frac{1}{n}} > [\mu(A)]^{\frac{1}{n}} + [\mu(B)]^{\frac{1}{n}}. \tag{13}$$

Let $t_i := \cos r_i$, the vector $\mathbf{t} := (t_1, t_2, \dots, t_k)$. The plane is defined as $\pi_i(p) := \langle p, p_i \rangle - t_i$. The intersection of the half spaces induced by the planes is $P(\mathbf{t})$. The central projection of $P(\mathbf{t})$ produces a spherical power diagram. The spherical area of each cell is denoted as $w_i(\mathbf{t})$. We define the space of \mathbf{t} as follows:

$$\mathcal{T} := \left\{ \mathbf{t} \mid \sum_{i=1}^{k} t_i = 1, w_i(\mathbf{t}) > 0, i = 1, 2, \dots, k. \right\}.$$

Lemma 5. The parameter space \mathcal{T} is a non-empty convex set in \mathbb{R}^k .

Proof. First, let t_i equal to $\frac{1}{k}$, then we obtain the spherical Voronoi diagram, $p_i \in W_i$, all the cells are non-empty. This shows $(\frac{1}{k}, \dots, \frac{1}{k})^T \in \mathcal{T}$, \mathcal{T} is non-empty.

Second, suppose $\mathbf{t}_1, \mathbf{t}_2 \in \mathcal{T}$, namely $w_i(\mathbf{t}_1) > 0$ and $w_i(\mathbf{t}_2) > 0$. For any $\lambda \in [0, 1]$,

$$P(\lambda \mathbf{t}_1 + (1 - \lambda)\mathbf{t}_2) = \lambda P(\mathbf{t}_1) \oplus (1 - \lambda)P(\mathbf{t}_2),$$

We use \tilde{w}_i to represent the polyhedron face area. It is obvious that $w_i > 0$ if and only if $\tilde{w}_i > 0$. According to Brunn–Minkowski inequality

$$\tilde{w}_i(\lambda \mathbf{t}_1 + (1-\lambda)\mathbf{t}_2)^{\frac{1}{2}} \geq \lambda \tilde{w}_i(\mathbf{t}_1)^{\frac{1}{2}} + (1-\lambda)(\tilde{w}_i(\mathbf{t}_2)^{\frac{1}{2}}) > 0.$$

Therefore $\lambda \mathbf{t}_1 + (1 - \lambda)\mathbf{t}_2 \in \mathcal{T}$, \mathcal{T} is convex. \square

Lemma 6. Suppose $\Omega \subset \mathbb{R}^n$ is a convex set, $f: \Omega \to \mathbb{R}$ is a C^2 strictly convex function (the Hessian matrix is positive definite everywhere in Ω), then the gradient mapping $\nabla f: \Omega \to \nabla f(\Omega)$ is a diffeomorphism.

We use this well-known lemma to prove the following theorem:

Theorem 4. Given a point set $\{p_1, p_2, ..., p_k\} \subset S^2$ in generic positions, given $\mathbf{t} \in \mathcal{T}$, construct the spherical power diagram $\mathcal{D}(\mathbf{t})$, where each cell area is $w_i(t)$. Obtain the mapping

$$\varphi: \mathbf{t} \mapsto \left(\frac{w_1}{t_1}, \frac{w_2}{t_2}, \dots, \frac{w_k}{t_k}\right)^T$$

is diffeomorphic.

Proof. Consider the closed differential 1-form,

$$\omega = \sum_{i=1}^k w_i(\mathbf{h}) dh_i = -\sum_{i=1}^k w_i(\mathbf{h}(\mathbf{t})) \frac{dt_i}{t_i},$$

the energy is defined as the integration of ω ,

$$E(\mathbf{t}) = \int^{\mathbf{t}} \omega,$$

then the gradient of the energy is

$$\nabla E(\mathbf{t}) = -\left(\frac{w_1}{t_1}, \frac{w_2}{t_2}, \dots, \frac{w_k}{t_k}\right)^T$$

From Eq. (9), the Hessian matrix element is

$$\frac{\partial^2 E}{\partial t_i \partial t_j} = -\frac{\partial}{\partial t_j} \frac{w_i}{t_i} = -\frac{1}{\sin \gamma_{ij}} \left(\frac{R_l^2 \sin d_l}{\cos^2 d_l} + \frac{R_k^2 \sin d_k}{\cos^2 d_k} \right) \tag{14}$$

$$\frac{\partial^2 E}{\partial t_i^2} = -\sum_{i \neq i} \frac{\partial^2 E}{\partial t_i \partial t_j}.$$

Similar to Eq. (11), we replace $\sin d_k$ and $\sin d_l$ with C = $\int_{d_{\nu}} \mu(\theta, \phi) \cos \theta d\theta$ and $D = \int_{d_{\nu}} \mu(\theta, \phi) \cos \theta d\theta$ to get the following formulae in the situation that the source measure is not

$$\frac{\partial^2 E}{\partial t_i \partial t_i} = -\frac{\partial}{\partial t_i} \frac{w_i}{t_i} = -\frac{1}{\sin \gamma_{ii}} \left(\frac{R_l^2 \cdot D}{\cos^2 d_l} + \frac{R_k^2 \cdot C}{\cos^2 d_k} \right) \tag{15}$$

$$\frac{\partial^2 E}{\partial t_i^2} = -\sum_{i \neq j} \frac{\partial^2 E}{\partial t_i \partial t_j}.$$

In both situations, the Hessian matrix is diagonally dominant with positive diagonal elements. Therefore, the energy is strictly convex on \mathcal{T} . By Lemma 6, the gradient mapping is diffeomorphic.

4.2. Computational algorithm

The variational formulation of spherical optimal transportation problem in previous section leads to an efficient algorithm. The energy $E(\mathbf{h})$ can be minimized with Newton's method.

The input to our algorithm is a topological sphere. Harmonic map, conformal for spherical case, is first applied to map the input to a unit sphere, and the mapping is well known for the uniqueness up to a Möbius transformation. Furthermore, the conformal factor of such conformal map gives a direct measure of area distortion. Our aim is to eliminate area distortion. For efficient spherical harmonic map algorithms, please see [48] for more details.

Suppose M be a topological sphere, and M is mapped to the unit sphere $S_0(\mathbf{P}) \subset S^2$ by harmonic map, where **P** are the vertices' positions on S^2 . We can assign an optional measure μ on S^2 . Practically we assign μ a value at $p_i \in \mathbf{P}$ and regard μ as a piecewise linear function on S^2 . μ can be 1 everywhere in the simplest case, which is the default measure. The total measure $\int_{S^2} \mu$ can be obtained by numerical integration: on each spherical triangle, a three-points Gaussian numerical integration formula is used. The term "measure" also denotes the integral of μ on some region, which is the spherical area if $\mu = 1$. We use term "area" instead of "measure" at some place for clarity.

We then compute the power diagram of the unit sphere given **P** and some power radius **r**. The power diagram $\mathcal{V}(\mathbf{P},\mathbf{r})$ is a cell decomposition of S^2 . Such decomposition gives us a map:

$$T: W_i \mapsto p_i \quad \forall \ W_i \in \mathcal{V}(\mathbf{P}, \mathbf{r})$$

where each cell W_i of the power diagram is mapped to a point p_i .

Spherical power diagram is computed using Sugihara's algorithm [45], which translates the construction of a spherical power diagram to computing the corresponding convex hull, as shown in Fig. 8, with the time complexity $O(n \log(n))$.

The target measure ν is a Dirac measure: we assign a weight v_i at every p_i , i.e. $v = \sum_i v_i \delta(p - p_i)$. In order to compute a spherical area-preserving mapping, we set v_i to be the vertex area on original surface M, namely one-third of surrounding triangles' area at each vertex. The total area of M is normalized to then total measure of S^2 .

Input: Genus 0 closed surface M, source measure $\mu: \mathcal{S}^2 \mapsto \mathbb{R}^+$, target measure $\nu = \sum_{i=1}^k \nu_i \delta(p-p_i)$, such that $\sum_i \nu_i = \int_{\mathcal{S}^2} \mu$ **Output**: spherical area-preserving parameterization

Compute conformal map from M to unit sphere, obtaining $S_0(\mathbf{P})$; Compute vertices' area of M and normalize the total area to be $\int_{S^2} \mu$, obtain ν ;

Initialize the power radius $\mathbf{h} = (h_1, h_2, \dots, h_k) = (0, 0, \dots, 0);$ while true do

```
if \|\nabla E\| < \varepsilon then
   break;
end
Compute power diagram \mathcal{V} given S_0(\mathbf{P}) and \mathbf{h};
Calculate gradient \nabla E by Eq. (17);
Calculate Hessian matrix H by Eqs. (9) and (10) or Eq. (11)
depending on the source measure \mu;
Solve linear equation H \cdot \delta \mathbf{h} = \nabla E;
\lambda \leftarrow 1:
while true do
     Compute the power diagram V(\mathbf{P}, \mathbf{h} + \lambda \delta \mathbf{h});
     if \forall W_i \in \mathcal{V} not empty then
         break;
     end
\mathbf{h} \leftarrow \mathbf{h} + \lambda \cdot \delta \mathbf{h}
```

Compute the centroid of each power cell $\forall W_i \in \mathcal{V}(\mathbf{P}, h)$ **return** the mapping from each vertex v_i to the centroid of W_i

Algorithm 1: Spherical Area Preserving Parameterization

Initially the area of W_i may not equal to v_i . We adjust the height vector **h** by minimizing the energy

$$E(h_1, h_2, \dots, h_k) = \int_0^{(h_1, h_2, \dots, h_k)} \sum_{i=1}^k (w_i(\tau) - \nu_i) d\tau_i$$
 (16)

then we obtain an updated power diagram, in which W_i 's areas are closer to v_i 's. The gradient of the energy is given by

$$\nabla E = (w_1 - \nu_1, w_2 - \nu_2, \dots, w_k - \nu_k)^T$$
(17)

At the unique minimum point \mathbf{h}^* , $\nabla E(\mathbf{h}^*) = 0$, the corresponding power diagram gives us the desired optimal transportation map:

$$T^*: W_i \mapsto p_i^* \quad \forall \ W_i \in \mathcal{V}(\mathbf{P}, \mathbf{h}^*)$$

 $s.t. \int_{W_i} d\mu = \nu_i, \ i = 1, 2, \dots, k.$

Furthermore, we compute the centroids of the power cells, denoted as \mathbf{P}^* , then we map each field W_i to p_i^* , this gives an area-preserving spherical parameterization $M \mapsto \mathbf{P}^* \subset \mathcal{S}^2$.

Recall that ν are vertices' area on the original surface, $\int_{W_i} d\mu =$ v_i , i = 1, 2, ..., k, meaning that we find a partition of unit sphere such that each cell's area equal to original surface's vertices' area.



Fig. 9. Area-preserving parameterization of bunny model, left: bunny model; middle: initial conformal map; right: area-preserving map.

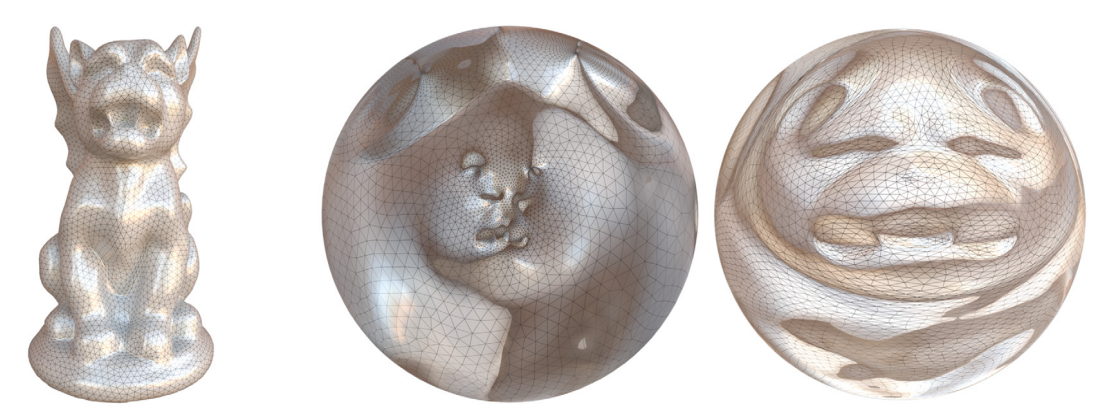


Fig. 10. Area-preserving parameterization of gargoyle model. left: gargoyle model; middle: initial conformal map; right: area-preserving map.

Computing the centroids of power cells, we obtain the target positions, which is the parameterization.

The convex energy $E(\mathbf{h})$ can be minimized by the Newton's method. Given initial height vector \mathbf{h} , we compute the spherical power diagram where $h_i = -\ln \cos r_i$, then compute the gradient in Eq. (17) and Hessian matrix in Eqs. (9) and (10), and update the height vector \mathbf{h} :

$$\mathbf{h} \leftarrow \mathbf{h} + \lambda H^{-1} \cdot \nabla E$$
.

The step length parameter λ is chosen such that all cells W_i of the power Diagram are non-degenerated. In practice, if some cells are degenerated, we reduce λ by half and recompute the power diagram, until all cells are non-degenerated. The algorithmic details for spherical area-preserving parameterization can be found in Algorithm 1.

Our algorithm is similar to the damped Newton's algorithm analyzed by Kitagawa et al. [49]. Theorem 1.5 in [49] claims that if some mild conditions are satisfied, such as

- the regularity, twist condition and Leoper's condition (Ma-Trudinger-Wang condition) of the cost function;
- the α-Holder continuity, the weighted Poincaré–Wirtinger inequality of the source density function;
- the compactness and the c-convexity of the support of the source measure,

then the damped Newton algorithm for semi-discrete optimal transport converges globally with linear rate and locally with rate $1+\alpha$.

In the algorithm, the spherical power cells should have positive mass at each iteration greater than ε . According to Theorem 4.1 in [49], this guarantees the regularity of the Kantorovich

potential to be $C^{2,\alpha}$, where α depends on the power cell masses ε , thus Newton's method can be performed.

Note that the target measure need not to be vertices' areas of original surface. In fact, it can be arbitrary as long as the total measure equals $\mu(\mathcal{S}^2)$. This flexibility enables us to compute not only area-preserving map but also area-controllable map. We can enlarge or shrink certain regions for better visual effects by setting the desired target measure.

Also note that we have constraints on the target point set p_i such that not all points are contained within any hemisphere. Otherwise, the dual convex polyhedron is not closed, resulting in some power cells with negative areas, and this will violate the regularity conditions of the Theorem 4.1 in [49].

5. Experiments and evaluation

In this section, we present some evaluation of our algorithm. We use pure Matlab to implement our algorithm and the experiments conducted on a laptop with 2.4 GHz CPU and 8 GB RAM. By setting target measure of vertices to be the normalized area of the input surface, our algorithm computes an area-preserving mapping from genus 0 surface to unit sphere.

In Fig. 9, the bunny model (left figure) is initially mapped to unit sphere with conformal mapping [32,33]. In the middle of center figure, the ear regions shrink seriously and are barely recognizable. Setting target area to be vertices' area of initial mesh, we obtain an area-preserving map, by Algorithm 1, as shown in the right figure. Now the ear region is parameterized nicely to observe its details.

We show two more experimental results in Figs. 10 and 14. Area elements of both models are well preserved as shown.

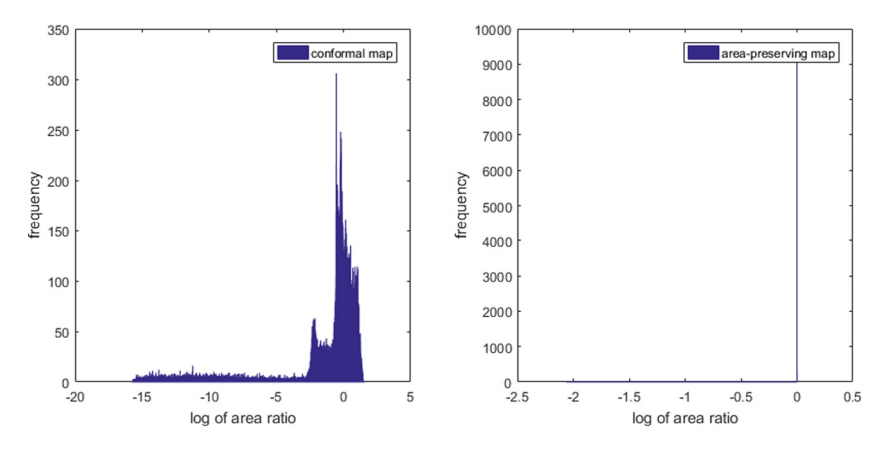


Fig. 11. Area distortion of bunny model. left: initial conformal map; right: area-preserving map.

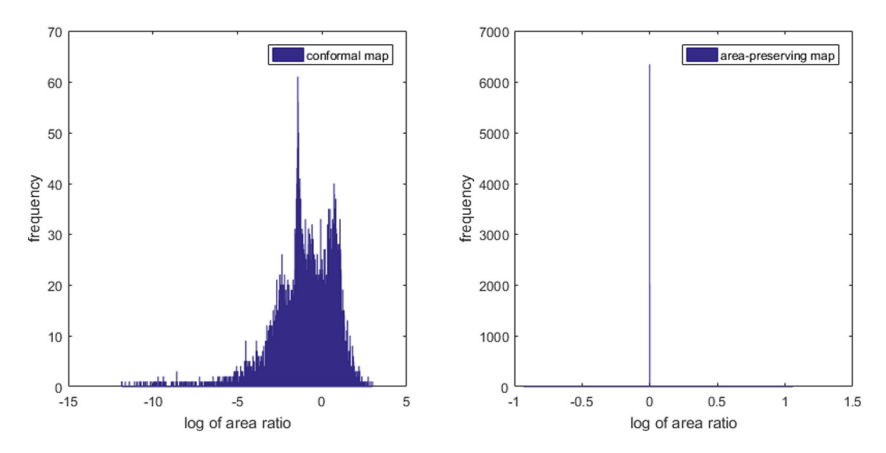


Fig. 12. Area distortion of gargoyle model. left: initial conformal map; right: area-preserving map.

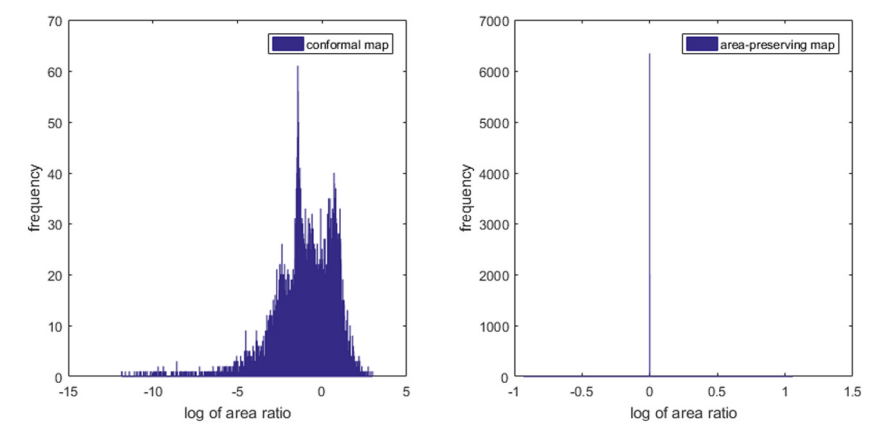


Fig. 13. Area distortion of Max Planck model. left: initial conformal map; right: area-preserving map.

For even more challenging models, like the lion and the horse shown in Fig. 15, traditional methods can introduce severe area distortion in the leg parts, as shown in the second column of Fig. 15. However, our algorithm manages to generate area preserving parameterization, shown in the third and fourth columns in Fig. 15, such that the feet and legs are still recognizable after the parameterization process.

Area distortion is measured by log of area ratio. Ideally this log area ratio should be equal to 0 for area-preserving parameterization. We show the histogram of area distortion for three models

in Figs. 11–13. It is clear that parameterizations of our algorithm preserves area accurately.

Running time of our algorithm is summarized in Table 1. We compute the optimal transport mapping to unit sphere for genus 0 surfaces. The number of iterations needed for convergence is generally not relevant to mesh size. Instead, it is more affected by the area distortion induced by the initial mapping (spherical conformal mapping in our case). As shown in Figs. 9 and 10, the initial area distortion (conformal factor) can be enormous when the input surface has ear-shape components.



Fig. 14. Numerical experiments. Top row shows the Maxplanck model, and skull and squirrel models are shown in the middle and bottom rows. The original input surface, conformal mapping results and area-preserving mapping results are shown in left, center and right column accordingly.

Table 1Performance statistics. 4th column is running time of our algorithm, 5th column is running time of Dominitz and Tannanbaum's algorithm [9]. 6th column is the speedup ratio.

Model	# vertices	# iter	Time (s)	Time* (s)	Ratio
Squirrel	2.5k	11	2.21	971	439.3
Gargoyle	10k	11	9.57	1451	151.6
Maxplanck	12.5k	6	5.29	2460	465.0
Skull	20k	5	6.9	2132	308.9
Bunny	35k	30	181	3093	17.1

In Table 1, we also compare the running time of our algorithm with algorithm of [9], as shown in fifth column. Our algorithm is generally tens to hundreds times faster. There are two factors contributing to such performance improvement. The first one is that our algorithm applies Newton's method while the algorithm in [9] is essentially gradient decent method. The second factor is

that the number of unknowns in our algorithm is |V| comparing to $|V|^2$ in [9].

6. Conclusion

In this paper, we generalized the semi-discrete optimal transportation theory from Euclidean geometry to spherical geometry, and applied it for spherical area-preserving parameterization.

The spherical optimal transportation map is given by a spherical power diagram, the powers can be obtained by optimizing a convex energy. We proved the existence and the uniqueness of the solutions, and give the explicit geometric interpretations to the gradient and the Hessian matrix of the energy. The variational theoretic framework leads to an efficient and robust algorithm for area-preserving parameterization.

Experiments show that our algorithm is able to compute areapreserving parameterization with high accuracy. Our algorithm is tens to hundreds time faster than previously developed algorithms.



Fig. 15. Numerical experiments on irregular meshes. Both models (first column) have long legs and are far from regular sphere shape, resulting in challenges for conformal parameterization (second column). Results from our method are shown in the third and fourth columns, where faces and legs are represented accordingly.

Acknowledgments

The authors acknowledge the support from National Natural Science Foundation of China (Grant No. 61772105, No. 61720106005, No. 61432003, No. 11001017), the National Science Foundation of the United States (Grant No. CMMI-1762287, DMS-1737812), the grant from Ford University Research Program (URP), USA (Award No. 2017-9198R). The authors are also grateful to anonymous referees for their helpful comments and suggestions.

Appendix

In this section, we will present some proof of the theorems and lemmas mentioned in previous sections in detail.

Proof of Lemma 1

Proof. Given a point $p \in W_i \cap \tilde{W}_i \triangleq W_{ii}$, then

$$-\ln\langle p, p_i\rangle - h_i \le -\ln\langle p, p_j\rangle - h_j$$

hence

$$\sum_{i} \int_{W_{i}} (-\ln\langle p, p_{i}\rangle - h_{i}) d\mu = \sum_{i} \sum_{j} \int_{W_{ij}} (-\ln\langle p, p_{i}\rangle - h_{i}) d\mu$$

$$\leq \sum_{i} \sum_{j} \int_{W_{ij}} (-\ln\langle p, p_{j}\rangle - h_{j}) d\mu = \sum_{i} \int_{\tilde{W}_{j}} (-\ln\langle p, p_{j}\rangle - h_{j}) d\mu$$

from measure-preserving condition,

$$\sum_{i} \int_{W_{i}} h_{i} d\mu = \sum_{i} h_{i} \mu(W_{i}) = \sum_{j} h_{j} \mu(\tilde{W}_{j}) = \sum_{j} \int_{\tilde{W}_{j}} h_{j} d\mu$$

the above is simplified to $C(V) \leq C(\tilde{V})$. \square

Proof of Lemma 2

Proof. As shown in Fig. 5, it is enough to show that $\{r_i, r_j, r_k\}$ determine $\{\theta_i, \theta_j, \theta_k\}$ analytically. In the spherical triangle $\Delta p_i q_k q_j$,

assume the arc lengths of p_iq_k and p_iq_j are α and β respectively, then by spherical cosine law

$$\cos \gamma = \cos \alpha \cos \beta + \sin \alpha \sin \beta \cos \sigma_i. \tag{18}$$

By spherical sine law,

$$\frac{\sin \sigma_i}{\sin \gamma} = \frac{\sin \angle 1}{\sin \alpha} = \frac{\sin \angle 2}{\sin \beta}.$$
 (19)

In the spherical triangle $\Delta q_k o q_i$, by spherical cosine law

$$\cos \theta_i = -\cos \angle 3 \cos \angle 4 + \sin \angle 3 \sin \angle 4 \cos \gamma$$

= $-\sin \angle 1 \sin \angle 2 + \cos \angle 1 \cos \angle 2 \cos \gamma$. (20)

By combining Eqs. (18)–(20), we can obtain the analytic formula for the inner angle θ_i , inside triangle $\Delta p_i p_j p_k$. We rewrite the angle θ_i as θ_i^{jk} , the cell area w_i equals

$$w_i = 2\pi - \sum_{ik} (\pi - \theta_i^{jk}).$$

This shows that w_i is an analytic function of the radius of vertex p_i and radii of vertices adjacent to p_i . \square

Proof of Theorem 1

Proof. As shown in Fig. 16, assume two cells W_i and W_j are adjacent. Suppose all circles are fixed except c_i , if r_i increases, $\cos r_i$ decreases, $h_i = -\ln\cos r_i$ increases, then w_i increases. Therefore, we have

$$\frac{\partial w_i(\mathbf{h})}{\partial h_i} > 0.$$

On the other hand, for all neighboring cells $w_j(\mathbf{h})$'s, the partial derivatives

$$\frac{\partial w_j(\mathbf{h})}{\partial h_i} < 0.$$

For all cells W_k 's which are not adjacent to W_i , $\partial w_k(\mathbf{h})/\partial h_i = 0$. Because the total area is fixed, we obtain

$$\sum_{j=1}^k \frac{\partial w_j(\mathbf{h})}{\partial h_i} = 0.$$

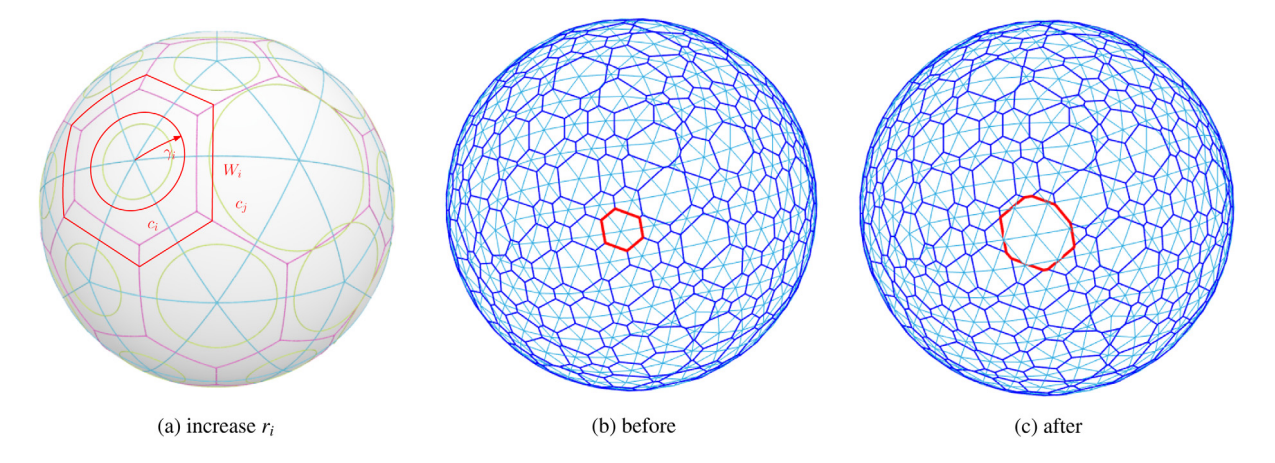


Fig. 16. The variation of a spherical power diagram, the cell W_i is enlarged by increasing r_i .

This shows the Jacobian matrix of the mapping $\varphi:\mathcal{H}\to\mathcal{W}$ has a null space spanned by $(1,1,\ldots,1)^T$. The space \mathcal{H} is orthogonal to the null space, therefore the Jacobian matrix is diagonal dominant. The matrix is non-singular on the space \mathcal{H} . Therefore, by implicit function theory, the mapping φ is locally diffeomorphic. \square

The proof of Lemma 3

To prove the correctness of Lemma 3, we directly use the following equations from Eq. (4):

$$\begin{cases} \gamma_i + \gamma_j &= \gamma_{ij} \\ \cos \gamma_i e^{h_i} &= \cos \gamma_j e^{h_j} \end{cases}$$
 (21)

Thus, we obtain

$$\begin{cases} \frac{d\gamma_i}{dh_j} = -\frac{R_{ijk}^2}{\sin\gamma_{ij}\cos^2 d_k}\cos r_i\cos r_j\\ \frac{d\gamma_i}{dh_j} = \frac{d\gamma_j}{dh_i} \end{cases}$$
(22)

By changing h_i to $h_i + \delta h_i$, γ_j shrinks to $\gamma_j - \delta \gamma_j$, then the power center moves from o to o_1 , shown in Fig. 6. The reduced region is illustrated as a blue spherical quadrilateral and a higher order infinitesimal triangle region. We use the following lemma to compute the area of the quadrilateral:

Lemma 7. As shown in Fig. 17, the area of the spherical quadrilateral is given by

$$\int_{\pi/2-\tilde{\theta}}^{\pi/2} \int_{0}^{\tilde{\phi}} \sin\theta \, d\phi \, d\theta = \tilde{\phi} \sin\tilde{\theta} \tag{23}$$

By Eqs. (22) and (23), the area of the quadrilateral colored in blue in Fig. 6 is

$$\sin d_k \delta \gamma_j = \sin d_k \frac{-R_{ijk}^2}{\sin \gamma_{ij} \cos^2 d_k} \cos r_i \cos r_j \delta h_i \tag{24}$$

Then we get Eq. (8). Furthermore, the formula is symmetric with respect to the indices i and j, hence we obtain

$$\frac{\partial}{\partial h_i} w_j^{ik} = \frac{\partial}{\partial h_j} w_i^{jk}$$

In the situation of non-constant source measure, namely $\mu=\mu(\theta,\phi)$, the measure of the quadrilateral colored in blue in Fig. 6 will become the following:

$$C \cdot \delta \gamma_j = C \cdot \frac{-R_{ijk}^2}{\sin \gamma_{ij} \cos^2 d_k} \cos r_i \cos r_j \delta h_i$$
 (25)

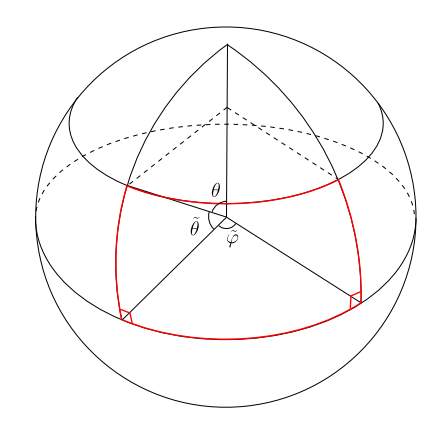


Fig. 17. Spherical quadrilateral.

where $C=\int_{d_k}\mu(\theta,\phi)\cos\theta d\theta$, the (θ,ϕ) is the local coordinate chosen such that the iso- θ curve and iso- ϕ curve are orthogonal and d_k lies on the iso- ϕ curve while γ_{ij} lies on the iso- θ curve. In general, we are replacing $\sin d_k$ in Eq. (24) with $\int_{d_k}\mu(\theta,\varphi)\cos\theta d\theta$.

References

- [1] Degener P, Meseth J, Klein R. An adaptable surface parameterization method. IMR 2003;3:201–13.
- [2] Zou G, Hu J, Gu X, Hua J. Authalic parameterization of general surfaces using Lie advection. IEEE Trans Vis Comput Graphics 2011;17(12):2005–14.
- [3] Brenier Y. Polar factorization and monotone rearrangement of vectorvalued functions. Comm Pure Appl Math 1991;44(4):375-417.
- [4] Alexandrov AD. Convex polyhedra. In: Springer monographs in mathematics, Berlin: Springer-Verlag; 2005.
- [5] Su Z, Zeng W, Shi R, Wang Y, Sun J, Gu X. Area preserving brain mapping. 2013, p. 2235–42.
- [6] Wang W, Ozolek JA, Slepcev D, Lee AB, Chen C, Rohde GK. An optimal transportation approach for nuclear structure-based pathology. IEEE Trans Med imaging 2011;30(3):621–31.
- [7] Arjovsky M, Chintala S, Bottou L. Wasserstein generative adversarial networks. in: International Conference on Machine Learning. 2017, p. 214–23.
- [8] Tolstikhin I, Bousquet O, Gelly S, Schoelkopf B. Wasserstein auto-encoders. 2017, arXiv preprint arXiv:1711.01558.
- [9] Dominitz A, Tannenbaum A. Texture mapping via optimal mass transport. IEEE Trans Vis Comput Graphics 2010;16(3):419–33.
- [10] Lévy B. A numerical algorithm for L2 semi-discrete optimal transport in 3D. ESAIM Math Model Numer Anal 2015;49(6):1693-715.
- [11] Su Z, Wang Y, Shi R, Zeng W, Sun J, Luo F, Gu X. Optimal mass transport for shape matching and comparison. IEEE Trans Pattern Anal Mach Intell 2015;37(11):2246–59.

- [12] Su K, Chen W, Lei N, Zhang J, Qian K, Gu X. Volume preserving mesh parameterization based on optimal mass transportation. Comput Aided Des 2017:82:42–56.
- [13] Nadeem S, Su Z, Zeng W, Kaufman AE, Gu X. Spherical parameterization balancing angle and area distortions. IEEE Trans Vis Comput Graphics 2017;23(6):1663–76.
- [14] Gu X, Luo F, Sun J, Yau S-T. Variational principles for Minkowski type problems, discrete optimal transport, and discrete Monge-Ampere equations. Asian J Math 2016;2(20):383–98.
- [15] Floater MS, Hormann K. Surface parameterization: a tutorial and survey. In: Advances in multiresolution for geometric modelling. Springer; 2005, p. 157–86.
- [16] Sheffer A, Praun E, Rose K, et al. Mesh parameterization methods and their applications. Found Trends Comput Graph Vis 2007;2(2):105–71.
- [17] Hormann K, Lévy B, Sheffer A. Mesh parameterization: Theory and practice. 2007.
- [18] Kantorovich L. On a problem of monge. Uspekhi Mat Nauk 1948;3:225-6.
- [19] Kantorovich LV. On a problem of Monge. J Math Sci 2006;133(4):1383.
- [20] ur Rehman T, Haber E, Pryor G, Melonakos J, Tannenbaum A. 3D nonrigid registration via optimal mass transport on the GPU. Med Image Anal 2009;13(6):931–40.
- [21] De Goes F, Cohen-Steiner D, Alliez P, Desbrun M. An optimal transport approach to robust reconstruction and simplification of 2d shapes. Comput. Graph. Forum 2011;30(5):1593–602.
- [22] De Goes F, Breeden K, Ostromoukhov V, Desbrun M. Blue noise through optimal transport. ACM Trans Graph 2012;31(6):171.
- [23] Mérigot Q. A multiscale approach to optimal transport. Comput. Graph. Forum 2011;30(5):1583–92.
- [24] Zhao X, Su Z, Gu X, Kaufman A. Area-preservation mapping using optimal mass transport. IEEE Trans Vis Comput Graphics 2013;19(12):2838–47.
- [25] Solomon J, Rustamov R, Guibas L, Butscher A. Earth mover's distances on discrete surfaces. ACM Trans Graph 2014;33(4):67.
- [26] Solomon J, De Goes F, Peyré G, Cuturi M, Butscher A, Nguyen A, Du T, Guibas L. Convolutional wasserstein distances: Efficient optimal transportation on geometric domains. ACM Trans Graph 2015;34(4):66.
- [27] Chen X, He H, Zou G, Zhang X, Gu X, Hua J. Ricci Flow-based spherical parameterization and surface registration. Comput Vis Image Underst 2013:117(9):1107–18.
- [28] Su Z, Zeng W, Wang Y, Lu Z-L, Gu X. Shape classification using Wasserstein distance for brain morphometry analysis. In: Information processing in medical imaging. Springer; 2015, p. 411–23.
- [29] Choi PT, Lam KC, Lui LM. FLASH: Fast landmark aligned spherical harmonic parameterization for genus-0 closed brain surfaces. SIAM J Imaging Sci 2015;8(1):67–94.
- [30] Haker S, Angenent S, Tannenbaum A, Kikinis R, Sapiro G, Halle M. Conformal surface parameterization for texture mapping. IEEE Trans Vis Comput Graphics 2000;(2):181–9.

- [31] Gu X, Yau S-T. Computing conformal structure of surfaces. 2002, arXiv preprint cs/0212043.
- [32] Gu X, Wang Y, Chan TF, Thompson PM, Yau S-T. Genus zero surface conformal mapping and its application to brain surface mapping. IEEE Trans Med Imaging 2004;23(8):949–58.
- [33] Lai R, Wen Z, Yin W, Gu X, Lui LM. Folding-free global conformal mapping for genus-0 surfaces by harmonic energy minimization. J Sci Comput 2014;58(3):705–25.
- [34] Lefèvre J, Auzias G. Spherical parameterization for genus zero surfaces using Laplace-Beltrami eigenfunctions. In: Geometric Science of Information. Springer; 2015, p. 121–9.
- [35] Aigerman N, Lipman Y. Orbifold Tutte embeddings. ACM Trans Graph 2015;34(6):1.
- [36] Jin M, Kim J, Luo F, Gu X. Discrete surface Ricci flow. IEEE Trans Vis Comput Graphics 2008;14(5):1030–43.
- [37] Kazhdan M, Solomon J, Ben-Chen M. Can mean-curvature flow be made non-singular?. 2012, arXiv preprint arXiv:1203.6819.
- [38] Friedel I, Schröder P, Desbrun M. Unconstrained spherical parameterization. J Graph GPU Game Tools 2007;12(1):17–26.
- [39] Zayer R, Rössl C, Seidel H-P. Curvilinear spherical parameterization. In: Shape modeling and applications, 2006. SMI 2006. IEEE international conference on. IEEE; 2006, p. 11.
- [40] Grimm CM. Simple manifolds for surface modeling and parameterization. In: Shape modeling international, 2002. Proceedings. IEEE; 2002, p. 237–44.
- [41] Praun E, Hoppe H. Spherical parametrization and remeshing. ACM Trans Graph 2003:22(3):340-9.
- [42] Asirvatham A, Praun E, Hoppe H. Consistent spherical parameterization. In: Computational science–ICCS 2005. Springer; 2005, p. 265–72.
- [43] Gotsman C, Gu X, Sheffer A. Fundamentals of spherical parameterization for 3D meshes. ACM Trans Graph 2003;22(3):358–63.
- [44] Saba S, Yavneh I, Gotsman C, Sheffer A. Practical spherical embedding of manifold triangle meshes. In: Shape modeling and applications, 2005 international conference. IEEE; 2005, p. 256–65.
- [45] Sugihara K. Laguerre Voronoi diagram on the sphere. J. Geom. Graph. 2002;6(1):69–81.
- [46] Wang X-J. On the design of a reflector antenna II. Calc Var Partial Differential Equations 2004;20(3):329–41.
- [47] Grünbaum B, Klee V, Perles MA, Shephard GC. Convex polytopes. Springer;
- [48] Gu XD, Yau S-T. Computational conformal geometry. Mass, USA: International Press Somerville; 2008.
- [49] Kitagawa J, Mérigot Q, Thibert B. Convergence of a Newton algorithm for semi-discrete optimal transport. 2016, arXiv preprint arXiv:1603.05579.